

Basestation 3-Dimensional Spatial Propagation Characteristics in Urban Microcell at 28 GHz

Tao Jiang, Lei Tian, Pan Tang, Zhixue Hu, Jianhua Zhang

Key Lab of Universal Wireless Communications, Ministry of Education,

Beijing University of Posts and Telecommunications, P. O. Box 92, Beijing 100876, China

Email: {jet, tianlbupt, jhzhang}@bupt.edu.cn

Abstract—This paper presents a millimeter wave channel measurement in Urban Microcell (UMi) scenario at 28 GHz with a bandwidth of 400 MHz. During measuring, a steerable horn antenna is used at receiver (RX) side while an omnidirectional antenna is used at transmitter (TX) side. The horn antenna not only rotates in azimuth with a step of 5° but also points into three different vertical angles. Based on the measured data, the 3-dimensional (3D) space characteristics of the millimeter wave channel are analyzed at the basestation (BS) side, e.g., azimuth angular spread of arrival (AASA), elevation angular spread of arrival (EASA) and their clustering results, by using the Space-Alternating Generalized Expectation-maximization (SAGE) algorithm and KPowerMeans algorithm. Through comparing the power angular profiles (PAPs) of raw data (RD) and SAGE results, the dynamic range of SAGE results will increase. The positive correlation between the measured distance and EASA is also investigated here.

Index Terms—channel measurement, channel statistical characteristics, 28 GHz, horn antenna, SAGE algorithm.

I. INTRODUCTION

With the increasing demand of high data rate communication, the millimeter wave (mmWave) communication technology which has abundant continuous spectrum resources has obtained more and more attention. On the world radio conference 2015 (WRC-15), some frequency bands above 6 GHz were regarded as the future candidate bands, such as 24.25-27.5 GHz, 31.8-33.4 GHz, 37-40.5 GHz, 40.5-42.5 GHz, 42.5-43.5 GHz, 45.5-47 GHz, 47-47.2 GHz, 47.2-50.2 GHz, 50.4-52.6 GHz, 66-76 GHz and 81-86 GHz. The federal communications commission (FCC) has adopted new rules to create a new Upper Microwave Flexible Use service in the 28 GHz (27.5-28.35 GHz). However, as the frequency increases, some characteristics of the radio propagation channel should be reexamined [1].

Conducting channel measurements in real communication environment is a reliable method to characterize the radio propagation channel. Based on the measured data, the statistic of channel parameters can be extracted, which provides insight into the design of mobile communication system. There are several universities and groups who have concentrated on modeling the radio propagation channel above 6 GHz and a great number of measurements have been carried out in different typical scenarios. The path loss is significantly high on mmWave band compared with that in the frequency band below 6 GHz [2][3]. In order to compensate the high path loss, high-gain directional horn antennas are used in the mmWave

measurements [4]. Besides, an omni-like virtual antenna array can be formed by rotating the horn antenna circularly [5]. T.S. Rappaport's team from NYU has conducted millimeter wave measurements at different bands, e.g., 28, 38, 60 and 73 GHz by rotating the horn antenna [6]. But, they mainly analyze the channel characteristics by the non-parameter method. Based on the measured data, power angular profiles (PAPs) can be obtained directly by processing the channel impulse responses (CIRs) or by using the Space-Alternating Generalized Expectation-maximization (SAGE) [7] results, in which the effects of antenna radiation pattern are removed from the CIRs [8]. However, the spatial characteristic results extracted by using the SAGE algorithm at basestation (BS) side are scarce. This mainly because the horn antenna is generally mounted at the user equipment (UE) side to conduct measurements conveniently. In this paper, we present a millimeter wave channel measurement which is carried out in Urban Microcell (UMi) scenario at 28 GHz with a bandwidth of 400 MHz. The horn antenna is placed on the rooftop of building as a BS. Based on the measured data, we apply SAGE algorithm to extracting the statistic of the millimeter wave channel characteristics including the azimuth angular spread of arrival (AASA) and elevation angular spread of arrival (EASA). Their clustering results are also obtained by using the KPowerMeans algorithm.

The rest of this paper is organized as follow. Section II shows the facility and measurement setting in Urban UMi scenario. Section III-A compares the two kinds of PAP calculated by raw data (RD) and SAGE algorithm separately. In Section III-B, we use the SAGE results to investigate angular spread of arrival (ASA) at each measured point. The 3-dimensional (3D) clustering results extracted by the KPowerMeans algorithm are presented in Section III-C. Finally, conclusions are given in Section IV to summarize the whole work.

II. FACILITY AND MEASUREMENT SETTING

The measurement campaign was conducted at the campus of the Beijing University of Posts and Telecommunications, which is a typical UMi scenario. A correlator sounder with a bandwidth of 400 MHz was used to capture the channel information. In terms of the antennas, a 2 dBi biconical antenna (360 degrees and 40 degrees half-power beamwidths in azimuth and elevation, respectively) was used at the transmitter

TABLE I
THE SPECIFICATIONS OF MEASUREMENT

Receiver	Transmitter	Range of Azimuth [°]	Range of Elevation [°]	Horizontal distance [m]	Rotation Nums	Scenario
RX1	TX1	-182 ~ -2	-10 ~ -30	6.0	111	NLoS
	TX2	105 ~ -75	-17 ~ -37	23.0	111	LoS
	TX3	95 ~ -85	-9 ~ -29	70.5	111	LoS
	TX4	92 ~ -88	-4 ~ -24	166.4	111	LoS
	TX5	90 ~ -90	-5 ~ -25	42.6	111	LoS
	TX6	90 ~ -90	-5 ~ -25	74.0	111	NLoS
	TX7	24 ~ -61	-4 ~ -24	48.4	168	LoS
	TX8	17 ~ -68	-5 ~ -25	63.0	168	LoS
	TX9	36 ~ -144	-7 ~ -27	87.3	111	NLoS
	TX10	3 ~ -177	-5 ~ -25	44.0	111	LoS
RX2	TX11	-6 ~ 174	-5 ~ -25	44.3	111	LoS
	TX12	-90 ~ 90	-25 ~ -45	16.7	111	LoS
	TX13	175 ~ 75	-22 ~ -42	9.3	150	NLoS
	TX14	-175 ~ 5	-4 ~ -24	46.2	111	LoS



Fig. 1. Layout of Measurement environment

(TX) side and mounted on a trolley as a UE. At the receiver (RX) side, a 25 dBi horn antenna (11 degrees and 10 degrees half-power beamwidths in azimuth and elevation, respectively) was used and mounted on the rooftop of a building as a BS. This building has a height of 13 m and it is surrounded by three tall buildings (15-storey, 55 m height). The height of antennas at UE and BS are 1.66 m and 13.38 m respectively. Fig. 1 shows the measurement environment.

At each measured location, the horn antenna was rotated at azimuth domain with the step of 5° and pointed into three different elevation angles with a spacing of 10°. The antenna response would not be changed during the rotation and it was calibrated in anechoic chamber. The scanning range of azimuth and elevation of each point are listed in Table I, and 100 CIRs will be recorded at each bore-sight angle of the horn antenna. To conduct measurements conveniently, two locations on the rooftop are chose as RX named RX 1 and RX 2. We assume that the east is the 0° in azimuth and horizontal plane is 0° in elevation. It should be noted that TX 1 and TX 13 are belong to NLoS because their vertical angle of view are out of the

scanning area.

III. MEASUREMENT RESULTS AND ANALYSIS

A. PAPs from RD and SAGE results

Generally, there are two typical methods to calculating the PAP based on the rotated-antenna measurements. The first one is using the received CIRs directly at each bore-sight angle of antenna, and the second way is using the SAGE results. To illustrate the rationality of SAGE results, we also plot the reconstructed PAPs in the picture, which is the product of SAGE results and antenna's response.

During the measurement, the received CIR at the n th pointing angle of horn antenna can be written as:

$$s_n(t) = \sum_l^L \alpha_l C_n(\varphi_l) \delta(t, \tau_l) + w_n(t), (n = 1, 2, \dots, N) \quad (1)$$

Where α_l , φ_l , τ_l donate the complex attenuation, angle of arrival and delay, respectively. The total number of propagation paths is represented by L and $w_n(t)$ is the complex additive white Gaussian noise signal. $C(\varphi)$ is the receiver antenna response at $\varphi = [\theta, \beta]$ where θ is the azimuth angle and β is the elevation angle. N is total rotation steps. Because the index n of step is corresponding to a bore-sight angle $\varphi_{bore} = [\theta_{bore}, \beta_{bore}]$, the CIR can also be written as $s_n(t, \varphi_{bore})$. By using the SAGE algorithm which is based on the maximum-likelihood criterion, we can extract the parameters of the propagation channel:

$$\Omega_l = [\alpha_l, \varphi_l, \tau_l; l = 1, 2, \dots, L] \quad (2)$$

To avoid the repetitive addition of colored noise, the calculation formula of azimuth PAP formed by RD is written as:

$$PAP(\varphi_{bore}) = \sum_{t \in T} \|s_n(t, \varphi_{bore})\|^2 \quad (3)$$

And the formula of azimuth PAPs formed by SAGE results

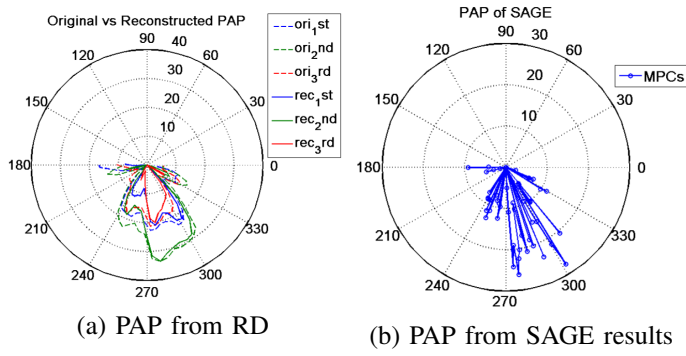


Fig. 2. PAP of TX 1

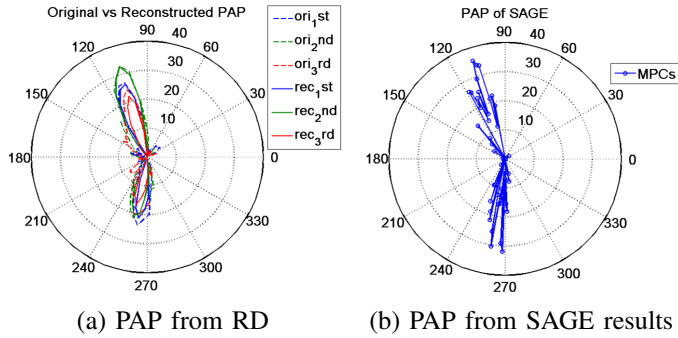


Fig. 3. PAP of TX 8

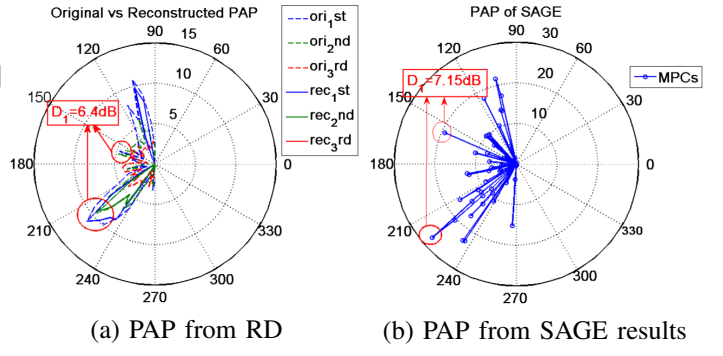


Fig. 4. PAP of TX 6

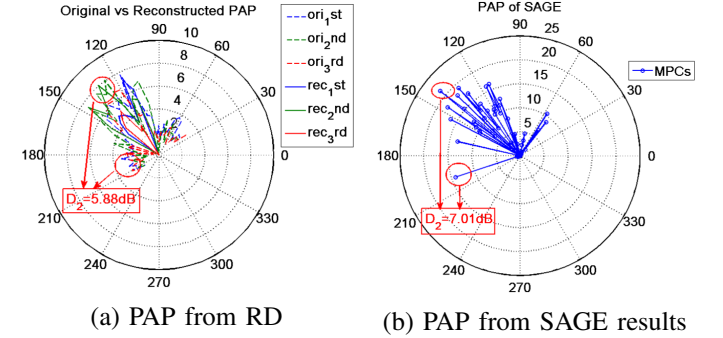


Fig. 5. PAP of TX 9

and the restored PAPs are written respectively in (4) and (5):

$$PAP(\varphi) = \sum_{t \in T} \sum_l^L \|\alpha_l \delta(t, \tau_l)\|^2 \quad (4)$$

$$PAP(\varphi_{bore}) = \sum_{t \in T} \sum_l^L \|\alpha_l C_n(\varphi_l) \delta(t, \tau_l)\|^2 \quad (5)$$

In Fig. 2~5, the PAPs of azimuth at TX 1, TX 8, TX 6 and TX9 are plotted in polar, respectively. In Fig. 2~5.(a), the PAPs calculated by RD are plotted in dashed line and the restored results are plotted in solid line. It should be noted that the results at three different elevation are plotted in three different colors respectively in same figure. Fig. 2~5.(b) depicts the PAPs composed by SAGE results. The radii of the polar means the dynamic range of each point.

There are two lobes in Fig. 3 which are caused by a directional path and a strong reflection path from Building 3. In NLoS scenarios like TX 6 and TX 9, the lobes are not big as that in LoS scenarios and their dynamic range is smaller correspondingly. From the PAPs results at the locations near BS like TX 1, we find that the width of lobes become larger and its dynamic range is similar to that under LoS condition. This is mainly because the distance between transmitter and receiver is very small, and the power of reflected rays decrease little in the distance.

As shown in Fig. 4~5, the dynamic range of PAPs calculated by RD is smaller than SAGE. This can be explained by that more tiny paths with slight energy are estimated in SAGE algorithm, which enlarge the dynamic area of PAPs. The above

investigations can also be proved by the results shown in Fig. 4 and Fig. 5. Comparing with the little variation of the power difference, the dynamic range changes sharply in these two methods, which illustrates the excellent performance of SAGE algorithm.

B. Directional RMS azimuth and elevation angular spread of arrival

The RMS angular spread of arrival plays an important role in wireless channel model and it is calculated as follow:

$$\Theta_{ASA} = \sqrt{\frac{\sum_{l=1}^L (\varphi_l - \mu_{ASA})^2 P_l}{\sum_{l=1}^L P_l}} \quad (6)$$

Where the P_l is the power of each path, μ_{ASA} is mean of the angle which is weighted by power P_l , and it is written as:

$$\mu_{ASA} = \frac{\sum_{l=1}^L \varphi_l P_l}{\sum_{l=1}^L P_l} \quad (7)$$

We use φ_{bore} and $PAP(\varphi_{bore})$ to calculate ASA from RD rather than using φ_l and P_l in equation (6) (7).

AASA and EASA of each measured point are shown in Table II. The subscript S and R represent the SAGE and RD respectively. To indicate the correlation among distance, AASA and EASA, these parameters are firstly normalized and plotted in Fig. 6. From Table II we can find the variation range of ASA calculated by RD is smaller than SAGE. This phenomenon is much more obvious when analyzing EASA.

The variation range of EASA calculated by SAGE results is from 3.64 to 9.73 but the value of EASA calculated by

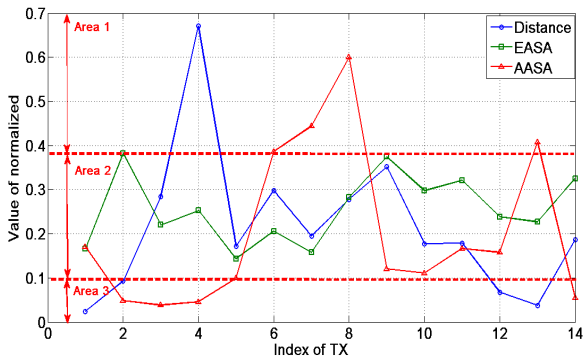


Fig. 6. ASA calculated by SAGE of each point

RD varies between 5.75 to 8.07. It can be seen from Fig. 6 that the values of AASA calculated by SAGE results can be divided into three areas which are distinguished in red dash line. As a typical measured point with strong reflection paths, the value of TX 6 is chosen as the boundary between Area 1 and Area 2. The value of TX 5 is the boundary between Area 2 and Area 3 because it is the separation point of LoS and NLoS scenarios. It can be seen from Table II that TX 2, 3, 4, 14 in LoS case which belong to Area 3 have lower AASA than others. In Area 1, although TX 7, 8 with strong reflection path are LoS points, they have the largest AASA. This situation can also be observed at TX 6 which is in NLoS scenario. Besides, Fig. 6 shows the correlation results between distance and EASA that the curve of the distance is exactly similar with EASA.

The above two phenomena can be illustrated by the definition of ASA. The value of ASA depends on the angular distribution and their power weight. For the first kind of phenomenon, the angle of the reflection path, which is far from the main lobe, will enlarge the variance of the angular distribution, and the intensive power of reflection path will magnify the power weight of this angle. In this case, the value of AASA will increase. For the second phenomenon, we limited the vertical scanning range during the measurement and this behavior would cause the distribution of elevation angle more centralized and the power weight will make considerable contribution to EASA.

Table III compares the statistic parameters of ASA obtained from our measurement and from the 3GPP TR 38.900. From the table we can see the AASA obtained from our measurement are smaller than that in 3GPP TR 38.900 but the mean value of EASA is similar under NLoS condition in 3GPP TR 38.900. This phenomenon is caused by the behavior that we mount the RX at the rooftop of building with height of 13 m and the reflection and scattering are mainly from the three tall buildings. Comparing with the complex environment near the ground, the number of reflection and scattering sources reduces sharply. Besides, the high altitude of the RX can also enrich the receiving paths from the vertical and the ESAS increases correspondingly.

TABLE II
ANGLE DISPERSION PARAMETERS OF DIFFERENT TRANSMITTER

Transmitter	$AASA_S$ [°]	$AASA_R$ [°]	$EASA_S$ [°]	$EASA_R$ [°]
TX1	21.35	35.45	4.22	7.09
TX2	6.02	29.39	9.73	7.93
TX3	4.81	43.63	5.60	8.07
TX4	5.76	20.72	6.43	7.86
TX5	12.44	39.30	3.64	7.47
TX6	48.24	52.82	5.24	7.22
TX7	55.49	72.38	4.01	5.75
TX8	74.95	74.20	7.18	7.68
TX9	15.05	35.60	9.53	7.82
TX10	13.83	36.41	7.57	7.86
TX11	20.84	33.25	8.17	7.57
TX12	19.69	31.95	6.06	6.30
TX13	50.91	55.10	5.78	6.59
TX14	6.93	23.58	8.28	7.43

TABLE III
COMPARATION WITH 3GPP

Scenarios		28GHz, here		3GPP TR 38.900	
		LoS	NLoS	LoS	NLoS
$\log_{10}(AASA_{SAGE}/1^\circ)$	μ	1.15	1.47	1.61	1.69
	σ	0.39	0.23	0.30	0.37
$\log_{10}(EASA_{SAGE}/1^\circ)$	μ	0.81	0.77	0.58	0.86
	σ	0.13	0.13	0.28	0.31

C. The characteristic of cluster

We applied KPowerMeans algorithm [9] to get the clustering results. Through analyzing the characteristic of clusters, we will no longer describe the azimuth and elevation separately and more detailed information of channels can be captured. The cluster results of TX 1 and TX 8 are showed in Fig. 7, and each color represent a cluster. The scale of the point in the picture signify the level of the power and the greater power, the larger size of the point. The comparison of cluster number and intra cluster ASA between the measurement and 3GPP TR 38.900 are shown in Table IV. It should be noted that, because of the limitation of narrow vertical scanning range, the angle distribution of clusters mainly depend on the azimuth.

The rotation range of horn antenna at RX 1 does not cover the directional path from TX 1, the clusters shown in Fig. 7(a) are thus actually caused by scatter components from the wall of Building 3. Most of the components distribute between -15° to -30° in elevation. But in Fig. 7(b), power of paths at elevation of TX 8 is more diffused. Another obvious difference is the cluster number. There are only 2 clusters at TX 8, but more than 6 clusters are divided at TX 1. It can be found the

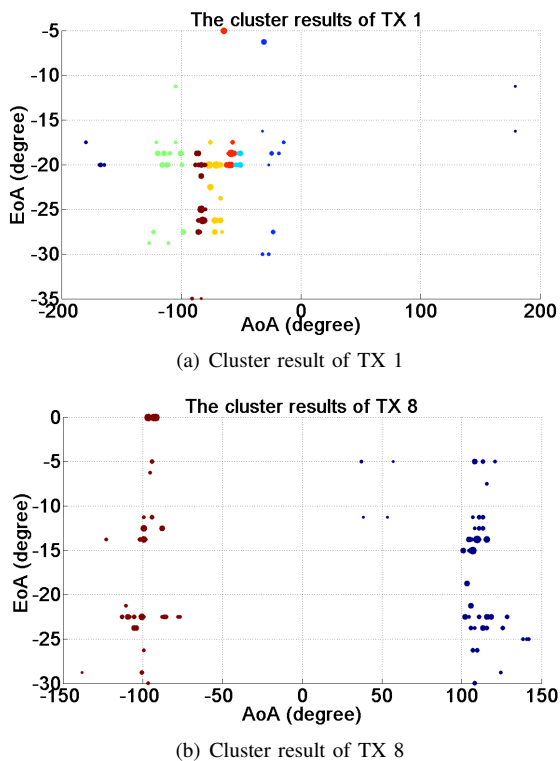


Fig. 7. Cluster result of each point

TABLE IV
COMPARATION WITH 3GPP

Parameters	28GHz,here		3GPP TR 38.900	
	LoS	NLoS	LoS	NLoS
Cluster Number	9.81	11	12	19
Inner-cluster AASA [°]	4.64	6.29	17	22
Inner-cluster EASA [°]	2.33	2.62	7	7

cluster numbers of other points, where have strong reflection paths, like TX 6, TX 7, are also limited by the number of reflection paths. From the statistical analysis of clustering at TX 8, we find that the elevation of the 2 cluster centers are -15° and -6° respectively. This suits well with the practical measurement. From Table IV we can find that the measured values are smaller than the reference value in standard. This may due to the scanning rang of the horn antenna dose not cover the all arrival directions of the paths.

IV. CONCLUSION

To conclude, we mainly analyze the arrival angle characteristic at BS side. The original data comes from the measurement, which is conducted in UMi environment at the center frequency of 28 GHz. The CIRs are obtained by the virtual antenna array that is developed by rotating horn antenna step by step. The SAGE algorithm and KPowerMeans algorithm are used to extract the statistic of the channel parameters. We find that the dynamic range of PAPs calculated with RD

is smaller than that by from SAGE results. This is because more paths with little power are estimated by SAGE. For the ASA of azimuth and elevation at BS side, the value of AASA will be enlarged if there are reflecting paths with strong power in the environment and the positive correlation between the EASA of BS and the distance is also be investigated. Equally important, it has been found that the AASA at BS side is smaller than that at UE side. Besides, the EASA is close to the typical value at UE side under NLoS condition by comparing the measured ASA with the reference value in 3GPP TR 38.900. Finally, the cluster results at BS side show that their angular characteristics have strong associations with the environment, especially when there are reflection paths caused by the surroundings, and the cluster number depends on the number of reflecting paths.

ACKNOWLEDGMENT

The research is supported in part by National Natural Science Foundation of China and project name is “Theoretical Modeling and Experiment Research of Propagation Channel” with NO. 61322110, and in part by National Science and Technology Major Project of the Ministry of Science and Technology and project name is “IMT-2020 Candidate Band Analysis and Evaluation” with 2015ZX03002008, and in part by 863 Program under Grant No. 2015AA01A703, and in part by Doctoral Fund of Ministry of Education (201300051100013).

REFERENCES

- [1] J. H. Zhang, P. Tang, and L. Tian, “The current and future of high frequency channel modeling,” in *Telecommunication Network Technology*, vol. 2016, pp. 10–17, 2016.
- [2] J. Lee, M.-D. Kim, J. Liang, J.-J. Park, and B. Park, “Frequency Range Extension of the ITU-R NLOS Path Loss Models Applicable for Urban Street environments with 28 GHz measurements,” in *2016 10th European Conference on Antennas and Propagation (EUCAP)*, pp. 1–5, April 2016.
- [3] F. Huang, L. Tian, Y. Zheng, R. Miao, and J. Zhang, “Propagation Characteristics of Mobile Channel in Urban Micro-Cells at 3.5 GHz and 6 GHz,” in *2016 IEEE 83rd Vehicular Technology Conference (VTC Spring)*, pp. 1–5, May 2016.
- [4] Y. Azar, G. N. Wong, K. Wang, R. Mayzus, J. K. Schulz, H. Zhao, F. Gutierrez, D. Hwang, and T. S. Rappaport, “28 GHz Propagation Measurements for Outdoor Cellular Communications Using Steerable Beam Antennas in New York city,” in *2013 IEEE International Conference on Communications (ICC)*, pp. 5143–5147, June 2013.
- [5] S. Hur, Y.-J. Cho, J. Lee, N.-G. Kang, J. Park, and H. Benn, “Synchronous Channel Sounder Using Horn Antenna and Indoor Measurements on 28 GHz,” in *Communications and Networking (BlackSeaCom), 2014 IEEE International Black Sea Conference on*, pp. 83–87, IEEE, 2014.
- [6] T. S. Rappaport, G. R. MacCartney, M. K. Samimi, and S. Sun, “Wideband Millimeter-Wave Propagation Measurements and Channel Models for Future Wireless Communication System Design,” *IEEE Transactions on Communications*, vol. 63, pp. 3029–3056, Sept 2015.
- [7] B. H. Fleury, M. Tschudin, R. Heddergott, D. Dahlhaus, and K. I. Pedersen, “Channel Parameter Estimation in Mobile Radio Environments Using the SAGE Algorithm,” *IEEE Journal on Selected Areas in Communications*, vol. 17, pp. 434–450, Mar 1999.
- [8] Y. Ji, x. yin, H. Wang, X. Lu, and C. Cao, “Antenna-De-embedded Characterization for 13-17 GHz Wave Propagation in Indoor Environments,” *IEEE Antennas and Wireless Propagation Letters*, vol. PP, no. 99, pp. 1–1, 2016.
- [9] C. Huang, J. Zhang, X. Nie, and Y. Zhang, “Cluster Characteristics of Wideband MIMO Channel in Indoor Hotspot Scenario at 2.35GHz,” in *Vehicular Technology Conference Fall (VTC 2009-Fall), 2009 IEEE 70th*, pp. 1–5, Sept 2009.